Non-uniform doping across the Fermi surface of NbS$_2$ intercalates

C. Battaglia[1], H. Cercellier[1], L. Despont[1], C. Monney[1], M. Prester[2], H. Berger[3], L. Forrò[3], M.G. Garnier[1], and P. Aebi[1]

[1] Institut de physique, Université de Neuchâtel, Switzerland
[2] Institute of physics, Zagreb, Croatia
[3] Institute of physics of complex matter, Ecole polytechnique fédérale de Lausanne, Switzerland

Abstract. Magnetic ordering of the first row transition metal intercalates of NbS$_2$ due to coupling between the conduction electrons and the intercalated ions has been explained in terms of Fermi surface nesting. We use angle-resolved photoelectron spectroscopy to investigate the Fermi surface topology and the valence band structure of the quasi-two-dimensional layer compounds Mn$_{1/3}$NbS$_2$ and Ni$_{1/3}$NbS$_2$. Charge transfer from the intercalant species to the host layer leads to non-uniform, pocket selective doping of the Fermi surface. The implication of our results on the nesting properties are discussed.

PACS. 79.60.-i Photoemission and photoelectron spectra – 71.18.+y Fermi surface: calculations and measurements

1 Introduction

Intercalation of the layered quasi-two-dimensional transition metal dichalcogenides is possible with a wide variety of electron donor species ranging from alkali metals [1] to large organic molecules [2]. The intercalation procedure is in general accompanied by charge transfer from the intercalant species to the host layer. This allows a fine tuning of the electron occupation of the relatively narrow d bands defining the Fermi surface of these compounds. Since the

Fig. 1. a) Fermi surface map of Mn$_{1/3}$NbS$_2$ at room temperature. The corresponding color scale is given in Fig. 2a). b) A sketch of the Brillouin zone of the host compound (full line) and of the $\sqrt{3} \times \sqrt{3}$ (dashed line) and 3×3 (dotted line) supercells with high symmetry points. High symmetry points in parenthesis are located on the top face of the hexagonal bulk Brillouin zone. The nesting vector corresponding approximately to the 3×3 superlattice is also indicated.

local bonding within the sandwiches is little changed upon intercalation, the changes in electronic properties are usually described within the rigid band model, in which the only change to the host material's electronic structure is the increased d band filling.

The first-row transition metal intercalation complexes are particularly interesting, because the d electrons left on the intercalate behave as localized atomic levels with a net magnetic moment, since there are no adjacent ions to allow overlap and band formation. Upon cooling, the local moments on these 3d ions exhibit a variety of magnetic orderings [3].

A direct exchange coupling between the moments has been ruled out because of their large spatial separation [4]. The anomalous behavior of the Hall coefficient and the resistivity near the magnetic transition temperature [5] suggests that the conduction electrons play a substantial role in mediating the exchange interaction between local moments via the Ruderman-Kittel-Kasuya-Yosida (RKKY) interaction [6,7,8]. In this indirect coupling mechanism, virtual transitions of the conduction electrons into the unoccupied orbitals of the 3d ion cause them to experience the direction of the intercalate moment and result in a local spin polarization of the conduction electron gas.

The response of the conduction electrons to the array of magnetic moments is determined by the static susceptibility $\chi(\mathbf{q})$, which depends on the details of the Fermi surface topology. This is the same susceptibility function which arises in the Fermi surface nesting criterion for charge density wave (CDW) formation [9]. Any singularity in $\chi(\mathbf{q})$ at a wavevector $\mathbf{q}$ will give rise to a spatial oscillation in magnetic polarization of the conduction electrons away
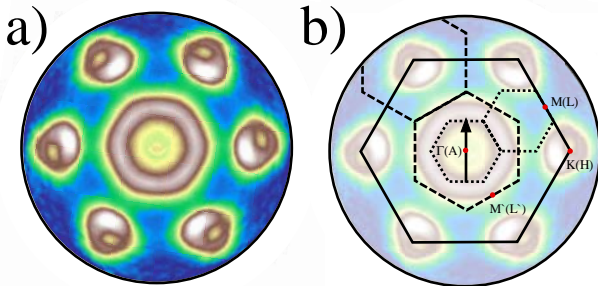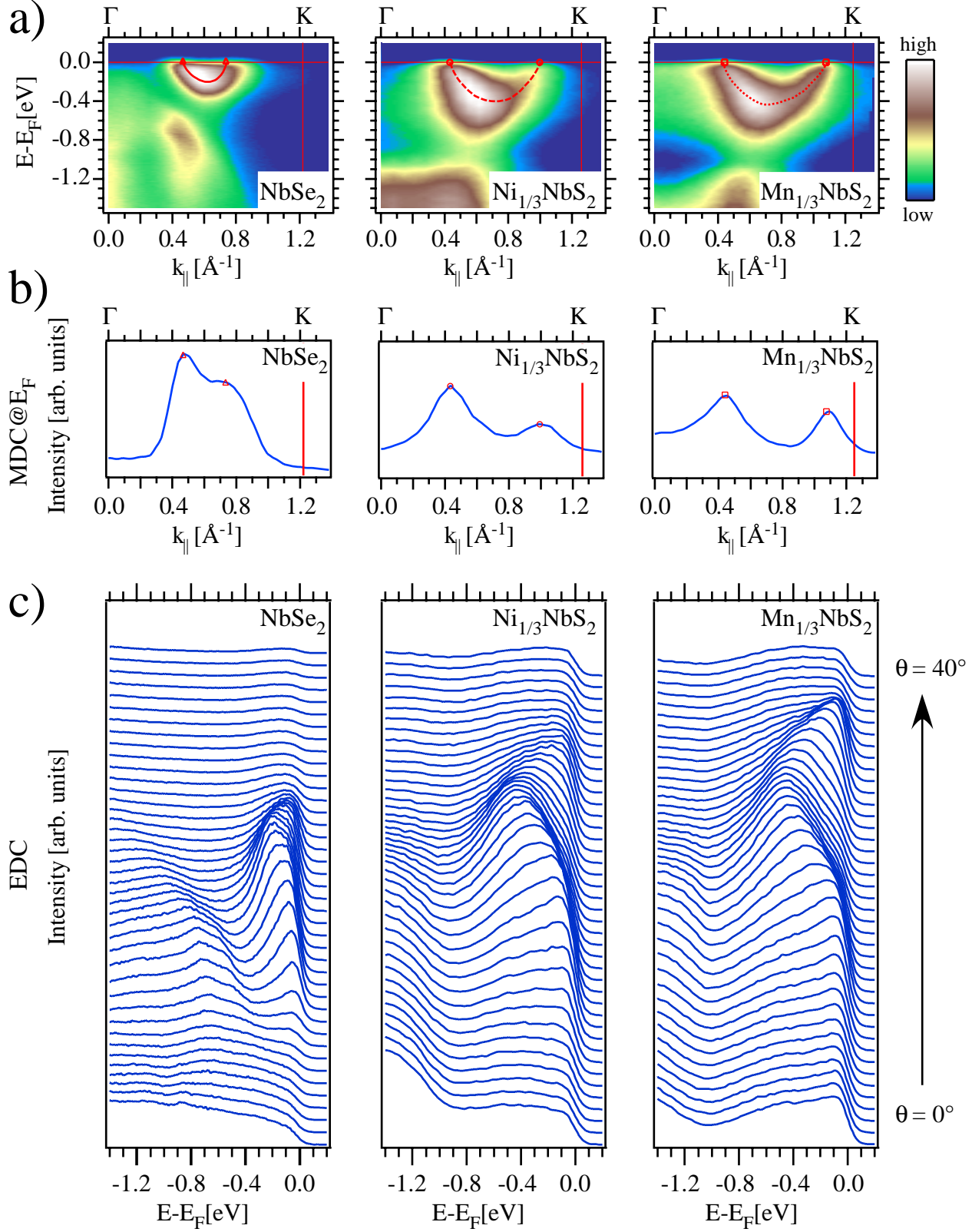
Fig. 2. a) Comparison between ARPES dispersion maps along the $\Gamma(A)-K(H)$ direction of NbSe$_2$, Ni$_{1/3}$NbS$_2$ and Mn$_{1/3}$NbS$_2$ measured at room temperature. b) MDCs extracted at the Fermi energy E_F as well as c) EDCs stacked as a function of emission angles θ are also shown. The red horizontal line marks the Fermi energy E_F, the red vertical line the position of the $K(H)$ point. To guide the eye, the dispersion of the Nb 4d band is outlined by red curves. The Fermi vectors obtained from the MDCs are marked by red symbols.

from the 3d ion. Depending on the spin response at the next 3d ion, the effective coupling may be ferromagnetic or antiferromagnetic.

Here, we report on a comparative angle-resolved photoelectron spectroscopy (ARPES) study of Mn$_{\frac{1}{3}}$NbS$_2$ and Ni$_{\frac{1}{3}}$NbS$_2$ above and below the magnetic phase transition temperature. Mn$_{1/3}$NbS$_2$ orders ferromagnetically at 40 K, while Ni$_{1/3}$NbS$_2$ orders antiferromagnetically at 90 K. We perform a direct mapping of the Fermi surface sheets and underlying band structure and compare our results to the data from 2H-NbSe$_2$. We find that the effect of intercalation leads to non-uniform doping of the Fermi surface across the Brillouin zone. We address the impact of our findings on the nesting behavior of the Fermi surface and discuss the validity of the rigid band approximation.

2 Experiment

ARPES experiments were performed in a modified Vacuum Generator ESCALAB Mark II spectrometer with a residual gas pressure of 2×10^{-11} mbar equipped with a Mg K$_\alpha$ ($\omega = 1253.6$ eV) x-ray anode, a discharge lamp providing monochromatized He Iα ($\omega = 21.2$ eV) radiation [10], and a three channeltron hemispherical electrostatic analyzer kept fixed in space during measurements. The samples were mounted on a manipulator with two rotational axes and may be cooled via a closed cycle refrigerator. Energy resolution is 20 meV, the combined angular resolution of sample manipulator and analyzer is approximately 1°. The different data acquisition modes are described elsewhere [11].

Crystals were grown by chemical vapor transport, mounted on the sample holders using conductive epoxy paste and cleaved in situ using an aluminum cleaving arm which was fixed onto the sample using epoxy paste. Despite the fact that the intercalated materials do not cleave as easily as non-intercalated compounds, we were able in this way to obtain mirror-like surfaces of sufficient quality. Surface cleanliness before and after ARPES measurements was monitored by x-ray photoelectron spectroscopy (XPS). Since the host compound 2H-NbS$_2$ was not available to us, we compare our data to isostructural and isoelectronic 2H-NbSe$_2$. A tight binding fit [12] to early non-selfconsistent band structure calculations [13] and our own calculations [14] show that the Nb 4d manifold defining the dominant parts of the Fermi surface is very similar for both compounds.

3 Results and discussion

Figure 1 shows the intensity distribution of photoelectrons for Mn$_{1/3}$NbS$_2$ collected from a small, resolution limited energy window centered on the Fermi energy E_F as a function of the surface-projected electron wave vector $\mathbf{k}_{||}$. The data has been averaged according to the space group P6$_3$22 [15] and was divided by a Gaussian shaped
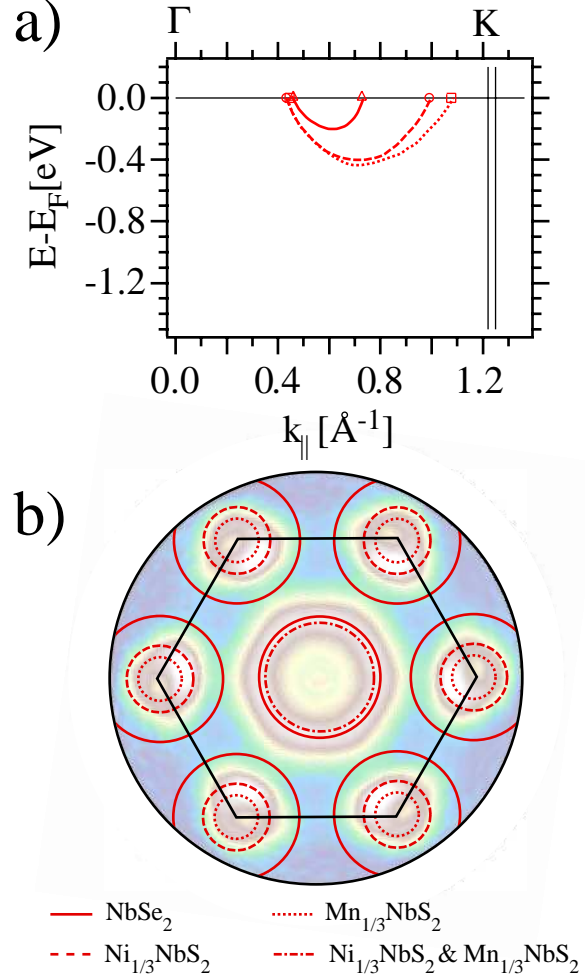
Fig. 3. Comparison between the Nb 4d band filling of NbSe$_2$, Mn$_{1/3}$NbS$_2$ and Ni$_{1/3}$NbS$_2$. a) Summary of the dispersion maps from Fig. 1a). Note the two positions of the K point due to the variation in lattice constant during intercalation. b) Sketch of the effect of doping on the Fermi surface.

background in order to enhance weaker off-normal emission features. Apart from a slight variation of the surface-perpendicular wave-vector $k_\perp$, this map corresponds to a horizontal cut through the Brillouin zone. It clearly reveals a rounded hexagonal Fermi surface sheet centered at $\Gamma(A)$ and a second approximately triangular sheet centered at $K(H)$. Both features are also observed for NbSe$_2$ [16] and Ni$_{1/3}$NbS$_2$ (not shown). First principles calculations [17] including our own [14] show that these features have predominantly Nb 4d character. For a strictly two-dimensional solid, the electronic dispersion is completely determined by $\mathbf{k}_{||}$, because there is no dispersion along $k_\perp$. Recent ARPES measurements have explored the $k_\perp$ dependence of the Fermi surface of NbSe$_2$ by varying the excitation energy and revealed a high degree of two dimensionality of the Nb 4d Fermi surface cylinders [18]. Because the unit cell of the host compound 2H-NbS$_2$ contains two formula units, all bands and hence the Fermi surface sheets are actually doubled. Their degeneracy is

lifted by interlayer coupling and spin-orbit interaction. Although the double-walled nature of the two Fermi surface sheets is not directly observed in the Fermi surface maps, it was shown earlier for NbSe$_2$ that the conduction band doublet is in fact resolvable by ARPES in energy distribution curves (EDC) [16]. However a full discussion of the lineshape of the spectral function of this class of materials is not subject of the present study and can be found in Ref. [11,19,9].

In Fig. 2a) we compare ARPES dispersion maps measured along $\Gamma(A) - K(H)$ of Mn$_{1/3}$NbS$_2$ and Ni$_{1/3}$NbS$_2$ with data from NbSe$_2$. Except for a sharpening of the Fermi edge, the spectra acquired below 20 K show the same behavior as the room temperature data within our angular and energy resolution. The color scale represents the intensity of the emitted photoelectrons plotted as a function of energy E and crystal momentum $\mathbf{k}_{||}$. Since the in-plane momentum of the photoelectron is conserved during the photoemission process, $\mathbf{k}_{||}$ of the electrons in the solid is obtained from the emission angle θ via $\mathbf{k}_{||} = \sqrt{2m(\omega + E - E_F - \phi_s)}sin\theta$ where m is the electron mass, ω the excitation energy and ϕ_s the sample work function [20]. Corresponding EDCs are shown in Fig. 2c). As a guide to the eye the dispersion of the Nb 4d band is outlined by red curves and summarized in Fig. 3a). Intensity at higher binding energy originates from S/Se 4p derived states. The Nb 4d band possesses an approximately parabolic dispersion for all three compounds. As expected within the rigid band picture, the main effect of the intercalation is the increased band filling reflected by a shift of the band bottoms of approximately 200 meV towards higher binding energies with respect to NbSe$_2$ for both intercalated compound. Simultaneously the dispersion parabola shifts away from the $\Gamma(A)$ point ($\theta = 0^o$) towards the $K(H)$ point ($\theta = 35^o$ for NbSe$_2$ and 36° for the intercalated compounds) violating the rigid band approximation. The locations of the Fermi crossings $\mathbf{k}_F$ were obtained by fitting two Lorentzian shaped peaks to the momentum distribution curves (MDC) extracted from the dispersion maps at the Fermi energy shown in Fig. 2b). It is interesting to note that the Fermi point at $\mathbf{k}_{||} = 0.44 - 0.46$ Å^{-1}, defining the size of the hexagonal hole pocket centered around the $\Gamma(A)$ point, is not affected by intercalation within our experimental resolution (our angular resolution of $\Delta\theta = 1^o$ translates into an uncertainty of $\Delta\mathbf{k}_{||} \leq 0.04$ Å^{-1}), whereas the second Fermi point strongly shifts towards the Brillouin zone border, causing the triangular pockets around $K(H)$ to shrink considerably. Thus intercalation leads to non-uniform, pocket selective doping of the Fermi surface, reducing the size of the $K(H)$ centered hole pockets, but leaving the occupation of the $\Gamma(A)$ pocket approximately unchanged. A sketch of this situation is shown in Fig. 3b). At present we are not able to explain why only the $K(H)$ pockets are doped.

Assuming a strictly two-dimensional dispersion and cylindrical hole pockets as shown in Fig. 3b), we estimate the electron filling of the Nb 4d band by computing the ratio between the area of occupied states and the area of

Table 1. Evolution of the Nb 4d band upon intercalation

compound	bottom of band [eV]	Fermi crossing $\mathbf{k}_F$ [Å^{-1}]	band filling [%]
NbSe$_2$	-0.2 eV	0.46, 0.74	0.63
Ni$_{1/3}$NbS$_2$	-0.4 eV	0.44, 1.00	0.79
Mn$_{1/3}$NbS$_2$	-0.4 eV	0.44, 1.08	0.82

the entire Brillouin zone. For the non-intercalated NbSe$_2$ compound we obtain a filling of 63 %. Due to the stochiometry and neglecting the bilayer splitting discussed before, therefore considering only one single band, the filling should be precisely 50 %. Our value is however reasonable since the existence of an additional small pancake shaped, Se derived, hole sheet centered around the $\Gamma(A)$ point is predicted by theory and has been confirmed by experiment [17,16,18]. The measured filling increases upon intercalation to 79 % and 82 % for the Ni and Mn intercalated compound respectively. In a simple ionic picture, assuming that Ni and Mn are divalent, the resulting d band filling of 5/6=83 % slightly overestimates the charge transfer from the intercalant to the Nb d band [21]. The valence state of the Ni and Mn ion determined from the band filling is +1.74 and +1.92 respectively. This behavior is consistent with the higher ionization energy of Ni with respect to Mn [22,23]. The valence state of +2.01 for the Mn ion derived from an earlier ARPES study [24,25] is also in good agreement with our result. Furthermore the multiplet splitting of the intercalant 3s core levels probed by x-ray photoemission spectra [24] is consistent with the adoption of an approximate +2 valence state of the magnetic ions. Numerical values concerning the evolution of the Nb 4d band upon intercalation are summarized in table 1.

We now address the issue of the validity of the doping description traditionally adopted for the interpretation of these compounds. Since in Mn$_{1/3}$NbS$_2$ and Ni$_{1/3}$NbS$_2$, the intercalant species occupy well defined interlayer sites forming a hexagonal $\sqrt{3}\times\sqrt{3}$ superlattice, one could alternatively interpret the intercalated compounds as stochiometric materials containing three formula units per unit cell. The superlattice gives rise to an additional periodic potential, which, within the Bloch theory of periodic crystals, is expected to fold back dispersion branches into the corresponding smaller Brillouin zone shown in Fig. 1. The relevance of this reduced zone scheme however remains unclear for a variety of compounds [9,26]. For the compounds under investigation, we do not find clear evidence for backfolding consistent with an earlier ARPES study [25] indicating that the superlattice potential is weak. We also note that the Nb 4d band minimum of the intercalated compounds does not fall on the M point of the new Brillouin zone, called M' in Fig. 1a), which is located halfway between the Γ and K point of the large Brillouin zone, violating the strict requirement of the Bloch theory that electron bands must cross the Brillouin zone with zero velocity. These observations thus support a description of the intercalation process via doping of the parent band

structure.

We now turn the discussion to the implications of the observed pocket selective doping on the nesting properties of the Fermi surface which via the susceptibility function determine the strength and range of the RKKY interaction. The doping independent $\Gamma(A)$ centered hexagonal hole cylinder provides a favorable topology for a threefold degenerate nesting vector directed along the $\Gamma - M$ direction corresponding approximately to a (3×3) superlattice in real space (see Fig. 1b). A (3×3) magnetic superlattice is commensurate with the $(\sqrt{3} \times \sqrt{3})$ superlattice formed by the intercalate moments and thus compatible with a magnetically ordered state. While the RKKY interaction decays isotropically as R^{-3} in the free electron case, $\mathbf{R}$ being the vector between two magnetic ions, the interaction becomes longer ranged for an anisotropic Fermi surface topology [27]. For the special case of a cylindrical region of the Fermi surface, the decay rate is governed by R^{-2} along the direction perpendicular to the axis of the cylinder. For two flat parallel regions of the Fermi surface, i.e. for ideal nesting conditions, the interaction is found to fall off only as R^{-1} in the direction perpendicular to the two planes. Furthermore, the sign of the RKKY coupling is modulated by $\sin(k_z - k_z')R$, where $\mathbf{k}$ and $\mathbf{k}'$ are two points on the Fermi surface and z is chosen along the R direction, allowing either antiferromagnetic or ferromagnetic coupling depending on the Fermi surface topology. However, if the RKKY interaction were the only important interaction and the relevant nesting took place within the $\Gamma(A)$ centered pocket, the magnetic behavior would be the same for both the Ni and the Mn intercalated compound. This is inconsistent with the experimental results since the Ni intercalates order antiferromagnetically, the Mn intercalates ferromagnetically. The nesting vector for the $\Gamma(A)$ centered sheet approximately coincides with the CDW vector observed by neutron scattering for NbSe$_2$ [28]. But because no evidence for a CDW-induced gap opening in ARPES spectra of NbSe$_2$ was found [16,18], the driving mechanism for the CDW transition has remained controversial and the simple nesting scenario has been questioned. It is instructive that in 2H-TaSe$_2$, which exhibits a similar Fermi surface topology, the CDW induced energy gap is nearly zero for the $\Gamma(A)$ centered sheet, although this sheet exhibits comparable nesting qualities as for NbSe$_2$. Instead the opening of a gap is observed on the $K(H)$ centered pocket [29]. This observation led to the suggestion [30] that the CDW state originates from the $K(H)$ centered sheet. Nesting across these pockets would possibly explain the occurrence of different magnetic orders, since the nesting vector depends on the band filling, which in turn depends on the intercalant species. However, since the cross-section of these cylinders are rounded triangles with flat edges oriented at 120° with respect to one another (see Fig. 1a), substantial nesting is highly unlikely. According to a recent first principle study for NbSe$_2$ [31] strong nesting occurs only between the flat triangular edges of the $K(H)$ pockets and the parallel flat edges of the central hexagonal pocket, resulting in a nesting vector along the $\Gamma - K$ direction. This nesting vector

would be doping dependent and could explain the variations in magnetic order. Based on the observation that the anomalies in the transport data for Ni$_{1/3}$NbS$_2$ are less pronounced than for Mn$_{1/3}$NbS$_2$, which indicates a weaker coupling of the conduction electrons to the magnetic moments, an alternative explanation has been considered: an additional superexchange interaction via the orbitals of the non-magnetic sulfur atoms is expected to lead to a predominantly antiferromagnetic coupling [5]. In this framework it is considered that the superexchange interaction is small for Mn intercalate, but becomes progressively larger as the intercalate is varied from Mn to Ni. The interplay between RKKY and superexchange interaction and the relevance of a nesting scenario should be revised taking into account our experimental observation of the doping dependence of the $K(H)$ pockets. For a final picture additional experimental data is required.

4 Conclusion

We have performed full-hemispherical Fermi surface mapping of Mn$_{1/3}$NbS$_2$ and Ni$_{1/3}$NbS$_2$ and validate the doping description of the intercalation process. Two hole pockets, one centered at the $\Gamma(A)$ point, the second centered at the $K(H)$ point are observed. Doping due to the intercalation of the host compound NbS$_2$ is non-uniform across the Brillouin zone and causes the $K(H)$ pockets to shrink, while the filling of the zone centered hole pockets remains surprisingly unchanged. Thus the rigid band model should be applied carefully and may only serve as a first approximation. The doping dependence of the nesting vector could possibly explain the different magnetic orders observed for the Mn and Ni compounds, but a simple nesting scenario does not appear to be sufficient for a complete picture and further complementary investigations are required.

5 Acknowlegdments

References

1. C.S. McEwen, D.J. St. Julien, P.P. Edwards, and M.J. Sienko. *Inorg. Chem.*, 24:1656, 1985.
2. F.R. Gamble, F.J. DiSalvo, R.A. Klemm, and T.H. Geballe. *Science*, 168:568, 1970.
3. S.S.P. Parkin and R.H. Friend. *Phil. Mag. B*, 41:95, 1980.
4. R.H. Friend, A.R. Beal, and A.D. Yoffe. *Phil. Mag. B*, 35:1269, 1977.
5. S.S.P. Parkin and R.H. Friend. *Phil. Mag. B*, 41:65, 1980.
6. A. Ruderman and C. Kittel. *Phys. Rev.*, 96:99, 1954.

7. T. Kasuya. *Progr. Theor. Phys.*, 16:45, 1956.

8. K. Yosida. *Phys. Rev.*, 106:893, 1957.

9. C. Battaglia, H. Cercellier, F. Clerc, L. Despont, M.G. Garnier, C. Koitzsch, P. Aebi, H. Berger, L. Forró, and C. Ambrosch-Draxl. *Phys. Rev. B*, 72:195114, 2005.

10. Th. Pillo, L. Patthey, E. Boschung, J. Hayoz, P. Aebi, and L. Schlapbach. *J. Electron Spectr. Relat. Phenom.*, 97:243, 1998.

11. F. Clerc, C. Battaglia, M. Bovet, L. Despont, C. Monney, H. Cercellier, M.G. Garnier, and P. Aebi. *Phys. Rev. B*, 74:155114, 2006.

12. N.J. Doran, B. Ricco, D.J. Titterington, and G. Wexler. *J. Phys. C: Solid State Phys.*, 11:685, 1978.

13. G. Wexler and A.M. Woolley. *J. Phys. C: Solid State Phys.*, 9:1185, 1976.

14. Our band structure calculations were performed in the framework of density functional theory using the full potential augmented plane wave plus local orbitals method in conjunction with the generalized gradient approximation as implemented in the Wien2k code by P. Blaha, K. Schwarz, G. Madsen, D. Kvansicka, and J. Luitz (Vienna University of Technology, Austria, 2002).

15. K. Anzenhofer, J.M. van den Berg, P. Cossee, and J.N. Helle. *J. Phys. Chem. Solids*, 31:1057, 1969.

16. Th. Straub, R. Claessen, Th. Finteis, P. Steiner, S. Huefner, C.S. Oglesby, and E. Bucher. *Physica B*, 259-261:981, 1999.

17. R. Corcoran, P. Meeson, Y. Onuki, P.-A. Probst, M. Springford, K. Takita, H. Harima, G.Y. Guo, and B.L. Gyorffy. *J. Phys.: Condens. Matter*, 6:4479, 1994.

18. K. Rossnagel, O. Seifarth, L. Kipp, and M. Skibowski. *Phys. Rev. B*, 64:235119, 2001.

19. F. Clerc, C. Battaglia, H. Cercellier, C. Monney, H. Berger, L. Despont, M.G. Garnier, and P. Aebi. *accepted for publication in J. Phys.: Condens. Matter*, 2007.

20. Due to a possible modification of the sample workfunction during the intercalation process, $\mathbf{k}_{||}$ slightly varies. However, for a typical value of the workfunction $\phi = 4$ eV with an associated error of $\Delta\phi = 1$ eV, variations of $k_{||}$ are below 3% and do not influence our conclusions.

21. In the purely ionic picture, the two chalcogen atoms per formula unit can fill their outer p shell by taking four electrons provided by the Nb atom. This leads to a d^1 configuration with a single electron left in the Nb d shell. Assuming a divalent state for the intercalant ion and taking into account that only $\frac{1}{3}$ of the ion is accounted for per formula unit, it contributes an additional $2 \times \frac{1}{3}$ electrons per formula unit to this band, leading to a total band filling of $\frac{1}{2}(1 + \frac{2}{3}) = \frac{5}{6}$, where the factor $\frac{1}{2}$ takes into account the fact that each band can accommodate two electrons.

22. R.H. Page and C.S. Gudeman. *J. Opt. Sco. Am. B*, 7:1761–1771, 1990.

23. J. Sugar and C. Corliss. *J. Phys. Chem. Ref. Data*, 14:1–664, 1985.

24. J.J. Barry and H.P. Hughes. *J. Phys. C: Solid State Phys.*, 16:L275, 1983.

25. J.J. Barry and H.P. Hughes. *J. Phys. C: Solid State Phys.*, 16:5393, 1983.

26. J. Voit, L. Perfetti, F. Zwick, H. Berger, G. Margaritondo, G. Gruener, H. Hoechst, and M. Grioni. *Science*, 290:501, 2000.

27. L.M. Roth, H.J. Zeiger, and T.A. Kaplan. *Phys. Rev.*, 149:519, 1966.

28. D.E. Moncton, J.D. Axe, and F.J. DiSalvo. *Phys. Rev. Lett.*, 34:734, 1975.

29. R. Liu, W.C. Tonjes, V.A. Greanya, C.G. Olson, and R.F. Frindt. *Phys. Rev. B*, 61:5212, 2000.

30. T. Valla, A.V. Fedorov, P.D. Johnson, P-A. Glans, C. McGuinness, K.E. Smith, E.Y. Andrei, and H. Berger. *Phys. Rev. Lett.*, 92:086401, 2004.

31. M.D. Johannes, I.I. Mazin, and C.A. Howells. *Phys. Rev. B*, 73:205102, 2006.